Research Square

Preprints are preliminary reports that have not undergone peer review.
They should not be considered conclusive, used to inform clinical practice,
or referenced by the media as validated information.

Resetting immunological tolerance in NMOSD via conformation-optimized AQP4-chimeric autoantibody receptor T cells

Jianmin Zhang

jzhang42@163.com

Institute of Basic Medical Sciences, Chinese Academy of Medical Sciences and School of Basic Medicine, Peking Union Medical College https://orcid.org/0000-0003-4765-0812

Yupeng Xu

Institute of Basic Medical Sciences, Chinese Academy of Medical Sciences and School of Basic Medicine, Peking Union Medical College

Menghua Cai

Institute of Basic Medical Sciences, Chinese Academy of Medical Sciences and School of Basic Medicine, Peking Union Medical College

Hexiang Yin

Peking Union Medical College Hospital

Yinghui Li

Institute of Basic Medical Sciences, Chinese Academy of Medical Sciences and School of Basic Medicine, Peking Union Medical College

Wenhua Qiao

Institute of Basic Medical Sciences, Chinese Academy of Medical Sciences and School of Basic Medicine, Peking Union Medical College

Mingyang Lu

Institute of Basic Medical Sciences, Chinese Academy of Medical Sciences and School of Basic Medicine, Peking Union Medical College

Lu Gao

Institute of Basic Medical Sciences, Chinese Academy of Medical Sciences and School of Basic Medicine, Peking Union Medical College

Yu Hu

Institute of Basic Medical Sciences, Chinese Academy of Medical Sciences and School of Basic Medicine, Peking Union Medical College

Hui Chen

Institute of Basic Medical Sciences, Chinese Academy of Medical Sciences and School of Basic Medicine, Peking Union Medical College

Yi Xu
Institute of Basic Medical Sciences, Chinese Academy of Medical Sciences and School of Basic Medicine, Peking Union Medical College
Yan Xu
Department of Neurology, Peking Union Medical College Hospital
Wei He
Institute of Basic Medical Sciences, Chinese Academy of Medical Sciences and School of Basic Medicine, Peking Union Medical College https://orcid.org/0000-0001-9444-5462

Article

Keywords: AQP4, NMOSD, CAAR-T cells, cell therapy, autoimmunology

Posted Date: October 24th, 2026

DOI: https://doi.org/10.21203/rs.3.rs-11213131/v1

License: This work is licensed under a Creative Commons Attribution 4.0 International License.
Read Full License

Additional Declarations: (Not answered)

Abstract

Neuromyelitis optica spectrum disorder (NMOSD) is a severe autoimmune channelopathy primarily driven by pathogenic autoantibodies against aquaporin-4 (AQP4). Current therapies, including broad B-cell depletion, often result in systemic immunosuppression and confer an increased risk of infectious complications. In this study, a precision immunotherapy platform was developed using chimeric autoantibody receptor (CAAR) T cells designed to selectively eliminate AQP4-reactive B cells. The CAAR construct incorporated M23 AQP4 (residues 1–232), preserving its native six-transmembrane topology and orthogonal array of particles organization. Binding assays using serum IgG from patients with AQP4-IgG-seropositive NMOSD confirmed that the M23 CAAR retained disease-relevant conformational epitopes. M23 CAAR-T cells exhibited antigen-specific activation, secreted IFN-γ and IL-2, and efficiently lysed engineered B cells expressing anti-AQP4 B cell receptors, while exhibiting minimally responsive to antigen-negative cells. A single infusion of M23 CAAR-T cells markedly reduced the target-cell burden and prolonged survival in systemic xenograft model of AQP4-reactive B cells. No discernible off-target toxicity was observed in antigen-negative control models or upon histopathological examination of major organs. Collectively, these findings demonstrate that M23 CAAR-T cells can selectively recognize and eliminate AQP4-reactive B cells, and they support the continued development of this approach as an antigen-specific cellular therapy for AQP4-IgG-seropositive NMOSD.

Introduction

Neuromyelitis optica spectrum disorder (NMOSD) is a severe, relapsing-remitting inflammatory channelopathy of the central nervous system (CNS) that primarily targets the optic nerves and spinal cord(1). Once considered a variant of multiple sclerosis, NMOSD was reclassified as a distinct disease after the identification of serum immunoglobulin G autoantibodies against aquaporin-4 (AQP4-IgG)(2, 3), with subsequent diagnostic refinements from the 2015 consensus criteria and myelin oligodendrocyte glycoprotein antibody-associated disease (MOGAD) recognitio(4, 5). NMOSD is globally prevalent with geographic and ethnic variation, being more common in African and Asian population(6, 7) and exhibiting a marked female bias (ratio > 9:1)(8). Clinically, recurrent attacks of optic neuritis, longitudinally extensive transverse myelitis, area postrema syndrome, and brainstem or cerebral syndromes can cause irreversible visual impairment, motor disability, and life-threatening respiratory failure(1, 9).

AQP4-IgG is both a diagnostic biomarker and a principal mediator of tissue injury in seropositive NMOSD. After the crossing blood–brain barrier, AQP4-IgG binds astrocytic AQP4 and activates complement- and antibody-dependent cytotoxicit(10–12). This astrocyte injury disrupts barrier homeostasis, triggering a cascade of inflammation, demyelination and neuronal loss(10, 13). B cells fuel this process through autoantibody production, antigen presentation, and cytokine secretion. NMOSD patients exhibit defective memory B-cell and plasmablast differentiation, with AQP4-reactive clones identified in peripheral blood and draining lymph nodes(14, 15). These findings support therapeutic targeting the pathogenic B-cell compartment.

Current AQP4-IgG-seropositive NMOSD treatments include terminal complement activation inhibitors (ravulizumab and eculizumab), B-cell lineage antibodies(rituximab), and interleukin-6 receptor signaling blocker(16–19). Despite improved disease control(20, 21), these therapies require repeated administration, lack selectivity for AQP4-reactive clones, and may compromise humoral immunity through broad B-cells depletion—as evidenced by increased hypogammaglobulinemia in long-term rituximab-treated NMOSD cohort(22). Moreover, CD20-directed therapy spares long-lived plasma cells, allowing relapse upon autoreactive B-cell reconstitution(15). These limitations underscore the need for more selective approaches that target pathogenic AQP4-specific B cells while preserving protective humoral immunity.

Chimeric antigen receptor (CAR) T-cell therapy offers durable B-cell depletion for severe autoimmune disease(23). CD19-directed CAR-T cells show efficacy in refractory systemic lupus erythematosus (SLE), systemic sclerosis, and idiopathic inflammatory myopathies(24, 25). However, their irrespective B-cell elimination and lymphodepleting preconditioning pose risks including cytopenias, hypogammaglobulinemia, infections, cytokine release syndrome, immune effector cell-associated neurotoxicity syndrome, and immune effector cell-associated hemophagocytic lymphohistiocytosis-like syndrome (IEC-HS)(23, 25, 26). Importantly, IEC-HS has also occurred in an early-phase clinical trial of CD19-directed CAR-T-cell therapy for SLE, indicating that this potentially life-threatening toxicity extends beyond oncology populations(27). In August 2026, autoimmune/neurological trials of CD19-CAR-T by Novartis were also paused after three fatal IEC-HS events, and Bristol Myers Squibb (BMS) voluntarily paused enrollment of zolacabtagene autoleucel trials after reversible inflammatory events were noted—underscoring the clinical relevance of these risks again(28, 29). These examples emphasize the distinct benefit–risk calculus for chronic autoimmune diseases versus fatal malignancies and the need for strategies that engage only disease-relevant while sparing protective lineage.

Whereas conventional CARs employ antibody-derived domains to bind lineage markers, Chimeric autoantibody receptor (CAAR) T present the autoantigen extracellularly to engage cognate B-cell receptor (BCR), thereby activating CAAR-T cells and selectively eliminate autoreactive B-cell clones. The concept was initially validated with desmoglein 3 CAAR-T cells in pemphigus vulgaris and later extended to additional preclinical models(30, 31), including those targeting muscle-specific tyrosine kinase and the N-methyl-D-aspartate receptor, demonstrating sparing of antigen-negative B cells(32, 33). CAARs provide an antigen-specific alternative to conventional CARs and could be a potential candidate for precise elimination of AQP4-reactive B cells in NMOSD without causing systemic immunosuppression and increasing the risk of infection.

AQP4-CAAR development faces unique challenges because the pathogenic epitopes of AQP4 depend on native membrane conformation and supramolecular assembly. AQP4 forms tetramers and M23 dependent orthogonal arrays of particles (OAPs)(34) and AQP4-IgG shows preferential binding to OAP-associated M23 over non-arrayed forms(35). Patient sera recognize native membrane-associated AQP4 tetramers and arrays more consistently than denatured proteins or isolated AQP4 fragments, supporting the importance of intact antigenic surface(36). Mutagenesis studies demonstrates that

pathogenic antibodies target discontinuous epitopes involving loops A, C, and E, while isolated loops are insufficient for complete recognition(37, 38). Moreover, antibody clustering on supramolecular AQP4 arrays facilitates multivalent C1q recruitment and classical complement activation, directly linking antigen organization to antibody pathogenicity(39). Cryo-electron microscopy(Cyro-EM) further revealed that patient-derived autoantibodies can recognize epitopes formed by multiple extracellular loops and, in some cases, by adjacent AQP4 molecules in assemblies(40). Thus, successful AQP4-CAAR design should preserve the native membrane topology and conformational epitopes recognized by the diverse patient AQP4-IgG repertoire.

Here, we developed an AQP4-CAAR-T-cell platform designed to selectively recognize and eliminate B cells expressing AQP4-reactive BCRs. The antigen-specific activation, cytokine production, proliferation, and cytotoxicity of the selected M23 CAAR-T cells were subsequently examined using engineered B-cell targets expressing patient-derived anti-AQP4 BCRs. Therapeutic activity was assessed in a systemic xenograft model of AQP4-reactive B cells, and potential antigen-independent and off-target toxicities were evaluated in vitro and in vivo. This work provides a preclinical assessment of conformation-dependent targeting of AQP4-reactive B cells and examines the feasibility of an antigen-specific cellular therapy for AQP4-IgG-seropositive NMOSD.

Results

1. Biological Information and Structural Basis for Targeting AQP4 in NMOSD

Before designing intervention strategies, a bioinformatic analysis of the AQP4 target antigen was conducted. To begin with, the GTEx transcriptome database was examined to assess the distribution of AQP4 across different organs. The results revealed a strong bias of AQP4 mRNA levels toward the central nervous system, with high signals in the cerebral cortex, cerebellum, and spinal cord **(**Fig. 1A**)**, while the expression in peripheral tissues, such as the heart, liver, and kidney were minimal or undetectable. The low expression level in non-CNS tissues provide a natural safety margin for systemic delivery, thus giving us a preliminary idea of the safe operating window at the molecular level. Structurally, AQP4 is a six-transmembrane (6-TM) water channel protein (Fig. 1B) that exists in two major translational isoforms: the full-length M1 and the N-terminally truncated M23 (Fig. 1C). A critical physiological feature of AQP4 is its supramolecular organization. Due to the long N-terminal domain causing spatial steric hindrance, the M1 isoform exists as a single tetramer, whereas the M23 isoform aggregates to form a highly ordered supramolecular structure known as orthogonal arrays of particles (OAPs) (Fig. 1C).

This spatial arrangement implies that if isolated peptide segments alone wre used as targeting units, the key conformational information required for antibody recognition is likely to be lost. Therefore, when constructing chimeric autoantibody receptors (CAARs), the three-dimensional framework of the native conformational epitopes in the extracellular domain was retained rather than resorting to truncated

linear epitopes. According to molecular modeling data, the former approach appeared to be more advantageous for simulating the interaction between autoantibodies and antigens.

2. Transcriptomic reprogramming of Patient B Cells Defines a Hyper-secretory Pathogenic Mechanism

To substantiate the clinical requirement for targeted B-cell depletion, a high-resolution transcriptomic analysis of B-lineage cells from NMOSD patients (GSE271586) was performed. Principal Component Analysis (PCA) revealed that the B cells from NMOSD patients exhibited significant and non-overlapping spatial segregation from the healthy control group. The main variation axes (PC1: 22.8%; PC2: 18.3%) indicated a fundamental reprogramming of the B-cell compartment (Fig. 1D). The transcriptomic split observed in our PCA was confirmed by the elevated expression of a specific B-cell gene set. Analysis of individual markers showed a significant increase in the levels of CD38, MZB1, and TNFRSF17 in NMOSD-derived B cells (Fig. 1E). These findings suggest that the patients' B cells have transitioned into a highly active state.

Functionally, the elevated expression of MZB1 and TNFRSF17 indicated that the B-cell pool was programmed for high-intensity antibody output. MZB1 facilitates immunoglobulin heavy-chain folding and antibody secretion as an endoplasmic reticulum-localized GRP94 co-chaperone, whereas TNFRSF17 (BCMA) mediates APRIL/BAFF-dependent prosurvival signaling in plasma cells(41, 42). The significant increase in these markers indicate that the patients' immune systems are preset to produce autoantibodies. To see if these changes were coordinated, we performed a correlation matrix analysis (Fig. 1F). The results revealed a strong positive correlation among all four genes, suggesting that they participate in a synchronized pathogenic process rather than acting independently. Such coordinated molecular evidence indicates that autoreactive B cells in NMOSD are not merely products of proliferation, but are biologically optimized for high-titer antibody synthesis. These findings on the distribution of AQP4 and B cell behavior provide a solid basis for the therapeutic strategy. By deploying M23 CAAR-T as a structurally precise "decoy," these hyperactive B-cell clones could be selectively eliminated.

3. Engineering Design and Clinical Recognition of AQP4-CAAR Structures

Based on the above structural principles, we designed two different CAAR architectures, "Tandem-Loop CAAR" and "M23 CAAR", to serve as molecular decoys for autoreactive B cells. The Tandem-Loop CAAR was constructed by linking the isolated extracellular loops A, C, and E in a linear arrangement to enhance epitope exposure, whereas the M23 CAAR employed a truncated M23 fragment (residues 1–232) that preserved the native six-transmembrane structure and the correct spatial arrangement of the conformational loops (Fig. 2A). For each antigen domain, the chimeric backbones were customized to ensure optimal surface stability and proper signaling. In the Tandem-Loop design, the loop sequences were appended to the CD28-derived hinge and transmembrane (TM) domains to provide structural support and membrane anchoring. By contrast, for the M23 CAAR, which natively carries its own six-transmembrane helices, the 4-1BB and CD3ζ signaling endodomains were fused directly to the C-

terminal end (residue 232) of the AQP4 scaffold, enabling the use of its endogenous TM regions for signal transduction (Fig. 2A).

We next investigated whether these constructs could be properly produced and anchored on the cell surface. Transient transfection of 293T cells yielded robust expression of all constructs, as evidenced by bright EGFP fluorescence signal (Fig. 2C). After surface localization was confirmed, the following investigation focused on whether these engineered receptors could recognize the authentic pathogenic antibodies in serum samples of patients. To this end, a “clinical-to-molecular” binding assay was performed by incubating the CAAR-expressing 293T cells with serum from AQP4-positive NMOSD patients. When tested, the Tandem-Loop CAAR showed no detectable binding above the background of healthy control levels (Fig. 2D, F), while the M23 CAAR design exhibited strong, high-affinity binding to the patient-derived autoantibodies (Fig. 2E, G). Quantitative analysis of multiple clinical samples confirmed that the natural conformation provided by the M23 scaffold was essential for recognizing pathogenic autoantibodies in NMOSD. This finding indicated that the pathogenic epitopes of AQP4 are strictly conformation-dependent and could not be reconstructed simply by using a linear sequence of loops. Accordingly, the M23 CAAR construct was selected as the sole candidate for all subsequent functional and therapeutic evaluations.

4. Generation of CAAR-T cells and Pathogenic B-Cell models

To estimate the translational potential of the molecular design above, engineered T cells and compatible target cells were established for *in vitro* functional conformation. Primary T cells were isolated from the peripheral blood of healthy donors and subjected to infection treatment with a gene delivery tool of the second-generation lentiviral vector. The efficiency of editing was confirmed by flow cytometry analysis on the 8th day after infection. The transduction rates of approximately 30% and 40% were observed for the CD19 CAR-T and the M23 CAAR-T groups, respectively, whereas the empty vector control group carrying the EGFP showed a positive rate exceeding 90% (Fig. 3A). These might because that the empty vector was relatively short in length, while the coding sequences for CAR and CAAR, along with the signal peptide, hinge region, and transmembrane domain, significantly increased the genetic load. Previous studies of lentiviral and γ-retroviral vectors have consistently shown that increasing vector genome length can reduce functional vector titer and transduction efficiency by impairing RNA packaging and subsequent steps of viral replication(43). Infection process was repeated in four independent healthy donors and the positive rates varied minimally among donors (Fig. 3B), suggesting that this difference was stable across individuals. Simultaneously, a "pathogenic B-cell" model was established to simulate the autoreactive B-cell clones found in NMOSD patients. A lentiviral transfer plasmid encoding a membrane-anchored, full-length human IgG-BCR based on the patient-derived AQP4-specific sequence D15107 (Fig. 3C) was conducted and connected to the cell surface via a CD5b transmembrane domain with mCherry and nanoLuciferase co-expressed for tracking and killing quantification. After transfecting this structural molecule into Nalm6 B cell line, fluorescence-activated cell sorting (FACS) was performed to enrich the target cell population. Following the procedure, the initially heterogeneous transfection products were converted into a highly uniform mCherry positive

population with purity exceeding 99% (Fig. 3D). This high-purity target population ensured that all subsequent functional data reflect antigen-specific interactions without being interfered by non-reactive cells.

5. M23 CAAR-T cells exhibit Selective Activation and Potent Cytotoxicity in Vitro

To evaluate the functional properties of the engineered effector cells, the T-cell cascade activation in M23 CAAR-T cells were examined after exposure to the target antigen. The Vector-T, CD19 CAR-T, and M23 CAAR-T cells were co-cultured respectively with the D15107-Nalm6 cell line expressing the target antigen for 16 hours. Changes in the expression of the early activation marker CD69 and the mid-late activation marker CD25 were detected by flow cytometry, The results showing that both the CD19 CAR-T and M23 CAAR-T groups exhibited significant upregulation of these markers, while the Vector-T group remained at resting levels (**Fig. 4A**). The activation dynamic results were consistent in four independent donors in repeated experiments (**Fig. 4B**). Therefore, the intensity of the signal transduction triggered by the M23 CAAR structure after binding to the targeted BCR was comparable to that of the clinically validated mature CD19 CAR structure. This had provided a foundation for the subsequent validation of effector functions such as cytotoxicity and cytokine secretion.

During the activation process, large amounts of pro-inflammatory cytokines were secreted. ELISA of co-culture supernatants revealed significantly increased concentrations of interferon-γ (IFN-γ) and interleukin-2 (IL-2) in the M23 CAAR-T group (**Fig. 4C**), while these cytokines were barely detectable in the Vector-T group supernatants. In the repeated experiments across four donors, the amounts of IFN-γ and IL-2 released by the M23 CAAR-T group remained consistently higher than those in the Vector control group and their secretion levels were comparable to those of conventional CD19 CAR-T cells.

The binding of CAAR receptors to the target antigen, as indicated by these results, not only caused an increase in activation markers on the T-cell surface but also droved downstream effector functions.

To define the therapeutic efficiency of our platform, we conducted a dose-titration cytotoxicity assay. When challenged with D15107-Nalm6 target cells, M23 CAAR-T cells exhibited a clear, dose-dependent trajectory of cell lysis. The killing efficacy increased steadily as the effector-to-target (E:T) ratio rose from 1:1 to 5:1, ultimately reaching a threshold of near-complete eradication (approximately 100% lysis) at a ratio of 10:1 (**Fig. 4D**).

The true clinical potential of CAAR-T cells lies in their ability to match the performance of existing benchmarks while offering superior safety. Therefore, we performed a comparison at the optimized E:T ratio of 10:1. The results demonstrated that the M23 CAAR-T cells possessed a cytolytic ability entirely comparable to that of the gold-standard CD19 CAR-T cells (**Fig. 4E**). While Vector-T and Blank-T cells remained quiescent, both M23 CAAR and CD19 CAR induced a clearance of the pathogenic B-cell model, suggesting that the "antigen-as-receptor" design does not compromise the inherent killing capacity of the T cells.

Finally, we conducted a critical specificity experiment to determine whether this potent killing could be restricted to pathogenic clones. When effectors were co-cultured with antigen-negative wild-type Nalm6 (Nalm6-WT) cells, a fundamental divergence in behavior was observed. CD19 CAR-T cells, acting as a broad-spectrum B-cell depleter, induced a near-total destruction of the WT cells. In contrast, M23 CAAR-T cells remained functionally silent, with cell viability levels identical to the Blank control group (**Fig. 4F**). This fundamental difference indicated that while CD19 CAR-T cells had a broad-spectrum ability to clear B cells, M23 CAAR-T cells could selectively eliminate pathogenic clones while preserving a broader, non-autoreactive B-cell repertoire.

6. M23 CAAR-T cells induce Rapid Clearance of Pathogenic B cells and extend Survival in Vivo

To evaluate the therapeutic efficacy of M23 CAAR-T cells in a complex biological environment, a systemic NMOSD xenograft model was established using immunodeficient NSG mice (Fig. 5A). On day 0, 6–8-week-old female NSG mice were intravenously inoculated with $1x10^6$ luciferase-labeled D15107-Nalm6 target cells to simulate systemic B-cell dissemination. On day 3, the mice were randomized into four groups and received a single intravenous injection of either PBS or $1×10^7$ effector cells (Vector-T, CD19 CAR-T, or M23 CAAR-T respectively). Bioluminescence imaging (BLI) was performed on days 7, 14, and 21 to track how the pathogenic B-cell burden changed over time and across different body regions **(**Fig. 5A**)**. During the observation, the PBS and Vector-T groups showed a steady and rapid increase in the luminescence signal in both the trunk and the limbs, suggesting a typical widespread pattern of B-cell. Meanwhile, the mice adopted the M23 CAAR-T infusion showed no obvious increase in luminescence **(**Fig. 5B**)**. When quantified the total flux got quantified from the BLI data, it was found that both the M23 CAAR-T and the CD19 CAR-T groups maintained significantly lower values at all the time points we measured **(**Fig. 5C**)**. These results provided further evidence for the M23 CAAR design possessing strong cell-killing activity *in vivo*.

As previously reported, sustained body-weight loss in tumor-bearing mice may accompany progressive disease and an increasing disease burden, whereas stabilization or recovery of body weight after treatment, together with reduced bioluminescent burden, is consistent with improved general condition following disease control(44, 45). Hence, the body weights of each treated groups were chosen as an indirect but sensitive measurement for assessing treatment-related systemic toxicity. The results showed that although the overall weights of all groups increased, the two groups treated with M23 CAAR-T or CD19 CAR-T treatment had significantly greater weight gain than the PBS and Vector-T control groups (Fig. 5D). No acute toxic signs were observed in the M23 CAAR-T group throughout the entire experiment – including no sudden weight drop, no reduced activity, nor abnormal behaviors such as piloerection – suggesting that the CAAR-T infusion at this dose did not trigger cytokine release syndrome or other off-target tissue damage.

Although tumor burden and cytokine release were relevant endpoints, the ultimate benchmark for clinical potential was whether this strategy would confer survival benefits in. The Kaplan-Meier survival curves showed that compared with the PBS group and the Vector-T cell control group, M23 CAAR-T cell therapy

significantly prolonged the survival time of mice (Fig. 5E). All the animals in the PBS group and the Vector-T group died successively within 40 days after tumor inoculation, while most of the mice that received a single infusion of M23 CAAR-T cells remained alive at the end of the observation window. The Log-rank test confirmed that the differences between the groups were significant (*P < 0.001*). Although the ultimate survival limits of all the animals had not been tracked in this experiment, the existing data suggested that M23 CAAR-T cells could specifically eliminate the pathogenic B-cell lineage in vivo, thereby achieving sustained remission and prolongation of survival.

7. In Vivo Specificity and Comprehensive Safety Profiling of M23 CAAR-T cells

A critical prerequisite for the clinical translation of CAAR-T therapy was to strictly restrict the cytolytic activity to the targeted-autoantibody-expressing B cells. To rigorously evaluate the specificity of M23 CAAR-T cells *in vivo*, we established a parallel "off-target" challenge model using wild-type Nalm6 cells (Nalm6-WT), which lack the D15107-BCR. Mice bearing either Nalm6-WT or D15107-Nalm6 target cells were treated with the same dose of M23 CAAR-T cells and compared by their disease progression. Longitudinal BLI revealed a fundamental difference in treatment efficacy: although M23 CAAR-T cells effectively cleared the BCR-expressing cells, the Nalm6-WT cells proliferated uncontrollably, showing a rapid increase in the bioluminescent signal identical to that of untreated controls (Fig. 6A). Statistical quantification of the total flux confirmed that the tumor burden in the Nalm6-WT group was significantly higher than that in the D15107-Nalm6 group (*P < 0.001*), indicating that M23 CAAR-T cells have no non-specific cytolytic activity *in vivo* (Fig. 6B).

In mice with Nalm6-WT cells, we observed a temporary increase of body weights in the early stage of the experiment, followed by a gradual decline. This pattern of an initial rise and subsequent decline was consistent with the tumor-induced cachexia. However, in the D15107-Nalm6 group treated with M23 CAAR-T, the weight curve showed a completely different trend: it steadily increased after the start of the treatment and remained stable throughout the follow-up period, without any signs of decline **(**Fig. 6C**)**. In terms of survival, M23 CAAR-T had no effect on extending the survival of the Nalm6-WT model. However, in the D15107-Nalm6 model, the same dose of CAAR-T treatment significantly prolonged the survival times, and the Log-rank test showed a significant difference between the groups (*P < 0.001*) (Fig. 6D). The only variable between the two experiments was the expression of the M23 CAAR recognized BCR configuration on the target cell, which was absent in Nalm6-WT but stably expressed in the D15107-Nalm6. This differential expression established that the observed weight recovery and survival benefit were attributable solely to antigen-specific recognition by CAAR-T cells, rather than to non-specific immune activation or graft-versus-host effects from the T cell infusion.

On day 24, mice from all four groups were euthanized so that a detailed histologic safety evaluation was carried out, the major vital organs, including the lungs, colon, heart, kidneys, and liver, were examined for signs of unintended toxicity against normal tissues or “on-target, off-tumor” effects. The results of Hematoxylin and Eosin (H&E) staining showed that all organs from the M23 CAAR-T-treated group had completely normal structures, with no inflammatory cell infiltration, cell death, or tissue damage

observed (Fig. 6E). Especially, the lungs, which normally expressing low level endogenous AQP4, also remained entirely intact. This result suggested that the activation threshold of the M23 CAAR-T cells had been properly tuned to avoid harming healthy tissues. Collectively, these findings indicated that the M23 CAAR-T cells had a favorable safety profile, supporting their promise as a targeted, well-tolerated precision therapy for NMOSD.

8. M23 CAAR-T cells serve as Precision Molecular Decoys that help reset Immunological Tolerance

A therapeutic model centered on M23 CAAR-T cells was proposed, based on comprehensive molecular, cellular, and *in vivo* data (Fig. 7). Under disease conditions, AQP4-reactive B-cell clones managed to escape immune tolerance and then differentiated into plasma cells, secreting large amounts of AQP4-IgG. After crossing the blood-brain-barrier, these antibodies could bind to AQP4 on astrocyte end-feet and subsequently recruit complement components as well as inflammatory cells, eventually causing demyelination, axonal damage, and neuronal dysfunction, which collectively underlined the clinical symptoms. In this model, however, the engineered T cells present the AQP4 autoantigen in its native M23 conformation on the surface, thereby acting as “molecular decoys”, allowing them to engage autoreactive B cells and plasmablasts through BCRs specifically with normal tissues unaffected. After the stable immune synapses formed between CAAR-T cells and the BCRs, the effector cells would be activated and expanded, releasing cytotoxic granules which selectively eliminate pathogenic B cells. This precision strategy had a distinct benefit for resetting the immune memory against AQP4 without wiping out the entire B-cell compartment or causing serious side effects. As a result, autoantibody titers would decrease, preventing further attacks and protecting the optic nerves and spinal cord, thus to offer a potentially curative option for patients with NMOSD.

Discussion

This study provides preclinical proof of concept for an AQP4-directed chimeric autoantibody receptor T-cell therapy for NMOSD. By incorporating M23-AQP4 into a CAAR, we applied the disease-associated autoantigen as a molecular bait to specifically recognize and eliminate B cells expressing anti-AQP4 B-cell receptors (BCRs). In contrast to conventional CAR-T cells targeting broad B-cell lineage markers, this strategy is designed to restrict cytotoxicity to autoreactive B cells. Patient-IgG recognition, antigen-dependent activation, selective cytotoxicity, in vivo target-cell clearance, and preliminary safety findings collectively support the feasibility of this antigen-specific approach.

The potential value of AQP4-CAAR-T cells lies in changing the level at which therapeutic selectivity is imposed. Broad B-cell- or plasma-cell-directed therapies can suppress autoantibody production but may also compromise protective humoral immunity, leading to B-cell aplasia, hypogammaglobulinemia, impaired vaccine responses, and infection. CAR-T therapy may additionally cause cytokine release syndrome, neurotoxicity, and hematologic toxicity. By recognizing the antigen specificity of the BCR rather than a shared lineage marker, AQP4-CAAR-T cells may provide a more restricted immune intervention suitable for a nonmalignant disease.

The performance of the M23 CAAR emphasizes the importance of preserving native autoantigen conformation. AQP4 is a six-transmembrane protein whose antibody-binding surface is formed by the spatial organization of extracellular loops A, C, and E within tetramers and higher-order orthogonal arrays of particles (OAPs). The inability of isolated extracellular-loop sequences to reproduce patient-IgG recognition indicates that these loops do not function as independent linear epitopes. Instead, their native spacing and orientation are required to reconstruct clinically relevant conformational epitopes. Patient-serum recognition of the M23 CAAR provides functional evidence that these epitopes are retained, although direct confirmation of tetramerization and OAP formation on the T-cell membrane remains necessary.

By using anti-AQP4 BCRs as recognition ligands, AQP4-CAAR-T cells could eliminate pathogenic memory B cells and surface-BCR-positive plasmablasts while sparing unrelated B-cell populations. This selectivity may help preserve immunoglobulin production and antimicrobial immunity. However, antigen-specific B-cell depletion should not yet be equated with restoration of immune tolerance. Long-lived plasma cells lacking surface BCR may escape recognition, while persistent autoreactive T-cell or newly generated AQP4-reactive clones could re-establish autoantibody production. Meanwhile, antigen-restricted recognition does not eliminate toxicity risk inherent to cellular immunotherapies. Accordingly, CAAR design must preserve pathogenic epitopes while avoiding antigen-independent activation, off-target recognition, and interference from circulating autoantibodies.

Further evaluation should also address the diversity of the autoreactive B-cell repertoire. The use of a defined anti-AQP4 BCR provides a controlled setting for demonstrating recognition, but cannot represent the full range of receptor affinities, epitope preferences, and surface expression levels encountered in patients. Testing primary patient-derived B cells would help determine how broadly the construct recognizes clinically relevant autoreactive populations. Parallel assessment of unrelated B cells and their functional responses would be needed to substantiate the proposed preservation of protective immunity. Such studies would clarify the relationship between antigen-specific targeting, depletion breadth, and the immunological consequences of this approach.

Normal AQP4-expressing tissues are not the intended targets of this CAAR because the receptor displays AQP4 and recognizes anti-AQP4 immunoglobulin expressed as a BCR. The absence of overt toxicity and organ pathology therefore provides initial evidence of tolerability but does not establish an absolute safety window. Circulating AQP4-IgG could occupy or crosslink the CAAR and affect T-cell activation, exhaustion, or target recognition. Moreover, CAAR-T cells may enter the central nervous system when the blood–brain barrier is disrupted, potentially producing either therapeutic effects or local inflammation. These possibilities require further investigation under physiologically relevant conditions.

Materials and Methods

Bioinformatics and Structural Modeling

The tissue-specific mRNA expression data of human *AQP4* were obtained from the Genotype-Tissue Expression (GTEx) portal (version 8) and the Human Protein Atlas (HPA). The data were normalized as Transcripts Per Million (nTPM).

Plasmid Construction and Lentivirus Production

The AQP4-CAAR constructs were designed by fusing either the tandem-linked extracellular loops (A, C, and E) to a CD28 hinge and transmembrane domain or the truncated M23 isoform (residues 1-232) of human AQP4 (UniProt: P55087), followed by CD137 (4-1BB) and CD3 ζ signaling endodomains, and a vector expressing only the EGFP fluorescent protein as a control. The CD19 CAR was designed by fusing CD19 HV and CD19 LV to a CD28 hinge and transmembrane domain, followed by CD137 (4-1BB) and CD3 ζ signaling endodomains as a positive control. The structures of the plasmids are shown in Fig. 2B.

The pathogenic B-cell receptor (BCR) model was constructed by cloning the light chain and heavy chain sequence through T2A of the AQP4-specific antibody D15107, fused to a CD5b-transmembrane anchor. The structure of the plasmid is shown in Fig. 3C. All constructs were inserted into a pLenti-EF1 α backbone co-expressing EGFP or mCherry/nano-Luciferase via P2A/T2A self-cleaving peptides.

In this study, the second-generation lentiviral packaging system was used to prepare the viral vectors required for all the engineered T cells. The packaging plasmid psPAX2 and the capsid plasmid pMD2.G provided the viral structural proteins and the envelope proteins respectively. These two plasmids were co-transfected with the recombinant lentiviral plasmid carrying the target gene at a molar ratio of 4:3:2, which was determined based on the previous titration optimization results, and it could achieve a good balance between the virus titer and packaging efficiency. The culture supernatant was collected 72 hours after transfection, and then concentrated by ultracentrifugation (5000×g, 4℃) and aliquoted for storage at -80℃. The aliquoting operation was designed to avoid the reduction in infectivity caused by repeated freezing and thawing.

Cell culture

The HEK293T and Nalm6 were purchased from the Cell Center of the Chinese Academy of Medical Sciences. HEK293T cells were cultured in DMEM (Gibco, San Francisco, CA, USA) containing 10% fetal bovine serum (Gibco, San Francisco, CA, USA). Nalm6 cells were cultured in RPMI 1640 (Gibco, San Francisco, CA, USA) medium containing 10% fetal bovine serum.

Human T cells were maintained in RMPI 1640 medium supplemented with HEPES (N-2-hydroxyethylpiperazine-N-2-ethanesulfonic acid)), sodium pyruvate, nonessential amino acids, and 2-mercaptoethanol (Thermo Fischer, Carlsbad, CA, USA). All the cells were incubated at 37℃ with 5% carbon dioxide.

Flow Cytometry

Before conducting the flow cytometry test, the cells were adjusted to the appropriate density according to the established experimental protocol, and simultaneous control groups of the same type and un-stained control groups were set up to define the positive threshold. After the cells were washed with PBS, they were incubated at room temperature with a blocking solution containing 1% BSA to block non-specific Fc receptor binding; then, the corresponding fluorescently labeled antibodies were added and incubated at 4°C in the dark for 30 minutes. After the incubation, the cells were washed with PBS three times again to remove unbound antibodies, and then the cells were resuspended in the buffer and loaded onto the flow cytometer for data collection. The entire staining process was carried out on ice to ensure the stability of cell viability and surface antigens.

Binding of patient serum IgG to AQP4-CAAR constructs

HEK293T cells were transiently transfected with plasmids encoding the M23-CAAR, Tandem-Loop-CAAR using polyethylenimine (408727, Sigma-Aldrich). Untransfected HEK293T cells were used as negative controls.

At 48 h after transfection, 1×10^5 cells from each group were collected and incubated with serum samples from patients with AQP4-IgG-seropositive NMOSD or healthy donors at a 1:10 dilution for 1 h on ice. After washing, the cells were incubated with an unconjugated Fc-specific goat anti-human IgG antibody (31125, Invitrogen; 1:200) for 20 min on ice. The cells were then washed and stained with Alexa Fluor 647-conjugated donkey anti-goat IgG (H + L) antibody (A-21447, Invitrogen; 1:800) and eBioscience Fixable Viability Dye eFluor 780 (65-0865-14, Invitrogen; 1:500) for 20 min on ice.

Samples were acquired by flow cytometry and analyzed using FlowJo software. This assay compared serum IgG binding to the two AQP4-CAAR designs using the same detection scheme. The analysis focused on viable single cells. Subtraction of the fluorescence measured in matched untransfected cells provided a background-referenced measure of binding for each indicated construct, rather than relying on its fluorescence intensity alone.

T Cell expansion in vitro

Primary human T cells were isolated from healthy donor PBMCs by lymphocyte separation medium. T cells were activated with anti-CD3/CD28 Dynabeads (Thermo Fisher) and cultured in RPMI-1640 medium supplemented with 10% FBS and 100 U/mL recombinant human IL-2. Activated T cells were transfected with CAAR or control (Vector/CD19 CAR) lentiviruses at a multiplicity of infection (MOI) of 3–10. Transfection efficiency was assessed by EGFP expression on Day 8 post-transduction. The expansion and engineering workflow therefore consisted of activation, lentiviral delivery, and assessment of reporter expression. EGFP expression at the stated time point was used to assess the efficiency of this process, with CAAR-engineered cells and the vector or CD19 CAR control cells included in the experimental design.

Generation of Pathogenic B-Cell Models

We constructed a lentiviral vector carrying the D15107-BCR-mCherry-nanoLuc fusion gene and transfected it into the human Nalm6 B cell line. To obtain target cells with uniform antigen expression density and sufficient expression level, we used the SH800S flow cytometer (SONY) to enrich the mCherry-positive cells. The sorted cells were re-tested by flow cytometry, and the positive purity reached over 99%, which was sufficient to eliminate the dilution effect that negative cells might cause on cytokine release or killing readings. The enrichment step reduced the proportion of reporter-negative cells in the target-cell population. Reassessment after sorting established the reported purity of the resulting population. This was relevant to subsequent functional assays because a mixed population containing negative cells could affect the interpretation of the measured responses.

Luciferase-based cytotoxicity

The cytolytic activity of CAAR-T cells was quantified using a luciferase-based killing assay. Nalm6 target cells stably expressing nanoLuciferase (nanoLuc) were inoculated into 96-well white-bottom plates. Effector T cells were added at indicated effector-to-target (E: T) ratios and co-incubated in phenol-free medium for 16 hours. At the endpoint, Nano-Glo substrate (Promega) was added according to the manufacturer's instructions. Bioluminescence was measured using a multimode plate reader. The percentage of specific lysis was calculated using the formula:

$$[1 - (\mathrm{Experimental\backslash:Group\backslash:RLU/Target\text{-}only\backslash:Control\backslash:RLU})] \times \ 100\%.$$

The target-only control provided the reference luminescence for calculating specific lysis. Experimental luminescence was expressed relative to this reference before conversion to a percentage. Under the stated formula, a lower experimental-to-control luminescence ratio corresponds to a higher calculated percentage of specific lysis.

Enzyme-Linked Immunosorbent Assay (ELISA)

After co-culture for 16 hours, the cell-free culture supernatant was collected and stored at -80°C until analysis. The concentrations of Interferon-gamma (IFN- γ) and Interleukin-2 (IL-2) were quantified using human ELISA kits according to the manufacturer's protocols. Briefly, 96-well plates were coated with capture antibodies overnight. After blocking, standards and samples were added, followed by incubation with detection antibodies and streptavidin-HRP. The reaction was developed with TMB substrate. The optical density (OD) was measured at 450 nm using a microplate reader. Cytokine concentrations were calculated based on the standard curves. The two cytokines were measured in supernatants collected at the stated co-culture endpoint. For each analyte, the standard curve was used to convert the measured optical density into a concentration. These measurements provided a soluble cytokine readout alongside the separate assessment of target-cell lysis.

In Vivo Therapeutic Efficacy and Safety

All anima experiments were approved by the Institutional Animal Care and Use Committee (IACUC). Female NSG mice aged 6 to 8 weeks were intravenously injected with $1x10^6$ D15107-Nalm6 target cells on Day 0. On Day 3, the mice were randomly divided into different groups and were given a single intravenous injection of $1x10^7$ M23 CAAR-T cells, CD19 CAR-T cells, Vector-T cells or PBS. Tumor burden was monitored by bioluminescence imaging (BLI) using the IVIS Spectrum system. Body weights were recorded every four days. For off-target assessment, a parallel control group was set up, inoculated with antigen-negative Nalm6-WT cells. At the study endpoint, major organs (heart, liver, spleen, lung, kidney, colon) were harvested for H&E staining to evaluate systemic toxicity.

Statistical Analysis

Statistical analyses were conducted using GraphPad Prism 9.0. The data were presented as mean ± SEM (standard error of the mean). Significant differences between groups were determined using unpaired two-tailed t-test. Survival curves were analyzed using the Kaplan-Meier method with log-rank tests. $P < 0.05$ was considered statistically significant. $P < 0.01$ was considered extremely significant. Group comparisons and survival analyses were evaluated using the respective tests specified above. The SEM described the uncertainty around the estimated mean, rather than the dispersion of individual observations. The stated P-value thresholds were used to interpret statistical significance.

Declarations

Competing interests

All authors declare that they have no commercial or financial ties that could pose a potential conflict of interest regarding this research.

Ethics approval and consent to participate

The experiment has been approved by the Ethics Committee of the Basic School of the Chinese Academy of Medical Sciences. (ID: ZS-1041). The animal experiment scheme was approved by the Experimental Animal Management and Ethics Committee of the Institute of Basic Medical Sciences, Chinese Academy of Medical Sciences, and all animal experiment operations met the animal ethical requirements. (ID: ACUC-2026-046).

Funding

This research was supported by the CAMS Initiative for Innovative Medicine (2025-I2M-KJ-012), the National Natural Science Foundation of China (32300745), the Key Research Program of Changzhou Xitaihu Development Foundation for Frontier Cell-Therapeutic Technology (2021-V-005).

Authors' contributions

MC, Yupeng Xu and JZ conceived the study and designed the experiments. Yupeng Xu and MC developed the methodology. Yupeng Xu, MC, YL, ML, WQ and LG performed the experiments. HY and YH provided research resources. Yupeng Xu and YL validated the experimental results. Yupeng Xu wrote the original draft of the manuscript. YX (Yi Xu), JZ, HC, WH and Yan Xu reviewed and edited the manuscript. JZ, WH, HC and Yan Xu supervised the study. JZ, WH, HC and YX (Yi Xu) secured funding.

Acknowledgements

We thank the staff of the Animal Laboratory Center at the Chinese Academy of Medical Sciences & Peking Union Medical College for assisting with the maintenance of the mice. We are also grateful to the Key Office of the School of Basic Medicine, CAMS & PUMC, for providing the research platform, and to all the faculty members for their dedicated support.

Availability of data and materials

Data supporting the present study are available from the corresponding author upon reasonable request.

References

1. Wingerchuk DM, Lucchinetti CF. Neuromyelitis Optica Spectrum Disorder. N Engl J Med. 2022;387(7):631–9.
2. Lennon VA, Wingerchuk DM, Kryzer TJ, Pittock SJ, Lucchinetti CF, Fujihara K, et al. A serum autoantibody marker of neuromyelitis optica: distinction from multiple sclerosis. Lancet. 2004;364(9451):2106–12.
3. Lennon VA, Kryzer TJ, Pittock SJ, Verkman AS, Hinson SR. IgG marker of optic-spinal multiple sclerosis binds to the aquaporin-4 water channel. J Exp Med. 2005;202(4):473–7.
4. Wingerchuk DM, Banwell B, Bennett JL, Cabre P, Carroll W, Chitnis T, et al. International consensus diagnostic criteria for neuromyelitis optica spectrum disorders. Neurology. 2015;85(2):177–89.
5. Banwell B, Bennett JL, Marignier R, Kim HJ, Brilot F, Flanagan EP, et al. Diagnosis of myelin oligodendrocyte glycoprotein antibody-associated disease: International MOGAD Panel proposed criteria. Lancet Neurol. 2023;22(3):268–82.
6. Hor JY, Asgari N, Nakashima I, Broadley SA, Leite MI, Kissani N, et al. Epidemiology of Neuromyelitis Optica Spectrum Disorder and Its Prevalence and Incidence Worldwide. Front Neurol. 2020;11:501.
7. Bagherieh S, Afshari-Safavi A, Vaheb S, Kiani M, Ghaffary EM, Barzegar M, et al. Worldwide prevalence of neuromyelitis optica spectrum disorder (NMOSD) and neuromyelitis optica (NMO): a systematic review and meta-analysis. Neurol Sci. 2023;44(6):1905–15.

8. Arnett S, Chew SH, Leitner U, Hor JY, Paul F, Yeaman MR, et al. Sex ratio and age of onset in AQP4 antibody-associated NMOSD: a review and meta-analysis. J Neurol. 2024;271(8):4794–812.
9. Wingerchuk DM, Hogancamp WF, O'Brien PC, Weinshenker BG. The clinical course of neuromyelitis optica (Devic's syndrome). Neurology. 1999;53(5):1107–14.
10. Papadopoulos MC, Verkman AS. Aquaporin 4 and neuromyelitis optica. Lancet Neurol. 2012;11(6):535–44.
11. Saadoun S, Waters P, Bell BA, Vincent A, Verkman AS, Papadopoulos MC. Intra-cerebral injection of neuromyelitis optica immunoglobulin G and human complement produces neuromyelitis optica lesions in mice. Brain. 2010;133(Pt 2):349–61.
12. Duan T, Smith AJ, Verkman AS. Complement-independent bystander injury in AQP4-IgG seropositive neuromyelitis optica produced by antibody-dependent cellular cytotoxicity. Acta Neuropathol Commun. 2019;7(1):112.
13. Lucchinetti CF, Mandler RN, McGavern D, Bruck W, Gleich G, Ransohoff RM, et al. A role for humoral mechanisms in the pathogenesis of Devic's neuromyelitis optica. Brain. 2002;125(Pt 7):1450–61.
14. Hoshino Y, Noto D, Sano S, Tomizawa Y, Yokoyama K, Hattori N, et al. Dysregulated B cell differentiation towards antibody-secreting cells in neuromyelitis optica spectrum disorder. J Neuroinflammation. 2022;19(1):6.
15. Damato V, Theorell J, Al-Diwani A, Kienzler AK, Makuch M, Sun B, et al. Rituximab abrogates aquaporin-4-specific germinal center activity in patients with neuromyelitis optica spectrum disorders. Proc Natl Acad Sci U S A. 2022;119(24):e2121804119.
16. Cree BAC, Bennett JL, Kim HJ, Weinshenker BG, Pittock SJ, Wingerchuk DM, et al. Inebilizumab for the treatment of neuromyelitis optica spectrum disorder (N-MOmentum): a double-blind, randomised placebo-controlled phase 2/3 trial. Lancet. 2019;394(10206):1352–63.
17. Pittock SJ, Berthele A, Fujihara K, Kim HJ, Levy M, Palace J, et al. Eculizumab in Aquaporin-4-Positive Neuromyelitis Optica Spectrum Disorder. N Engl J Med. 2019;381(7):614–25.
18. Traboulsee A, Greenberg BM, Bennett JL, Szczechowski L, Fox E, Shkrobot S, et al. Safety and efficacy of satralizumab monotherapy in neuromyelitis optica spectrum disorder: a randomised, double-blind, multicentre, placebo-controlled phase 3 trial. Lancet Neurol. 2020;19(5):402–12.
19. Kümpfel T, Giglhuber K, Aktas O, Ayzenberg I, Bellmann-Strobl J, Häußler V, et al. Update on the diagnosis and treatment of neuromyelitis optica spectrum disorders (NMOSD) - revised recommendations of the Neuromyelitis Optica Study Group (NEMOS). Part II: Attack therapy and long-term management. J Neurol. 2024;271(1):141–76.
20. Pittock SJ, Barnett M, Bennett JL, Berthele A, de Sèze J, Levy M, et al. Ravulizumab in Aquaporin-4-Positive Neuromyelitis Optica Spectrum Disorder. Ann Neurol. 2023;93(6):1053–68.
21. Tahara M, Oeda T, Okada K, Kiriyama T, Ochi K, Maruyama H, et al. Safety and efficacy of rituximab in neuromyelitis optica spectrum disorders (RIN-1 study): a multicentre, randomised, double-blind, placebo-controlled trial. Lancet Neurol. 2020;19(4):298–306.

22. Kim SH, Park NY, Kim KH, Hyun JW, Kim HJ. Rituximab-Induced Hypogammaglobulinemia and Risk of Infection in Neuromyelitis Optica Spectrum Disorders: A 14-Year Real-Life Experience. Neurol Neuroimmunol Neuroinflamm. 2022;9(5).
23. Schett G, Mackensen A, Mougiakakos D. CAR T-cell therapy in autoimmune diseases. Lancet. 2023;402(10416):2034–44.
24. Mackensen A, Müller F, Mougiakakos D, Böltz S, Wilhelm A, Aigner M, et al. Anti-CD19 CAR T cell therapy for refractory systemic lupus erythematosus. Nat Med. 2022;28(10):2124–32.
25. Müller F, Taubmann J, Bucci L, Wilhelm A, Bergmann C, Völkl S, et al. CD19 CAR T-Cell Therapy in Autoimmune Disease - A Case Series with Follow-up. N Engl J Med. 2024;390(8):687–700.
26. Hines MR, Knight TE, McNerney KO, Leick MB, Jain T, Ahmed S, et al. Immune Effector Cell-Associated Hemophagocytic Lymphohistiocytosis-Like Syndrome. Transplant Cell Ther. 2023;29(7):438.e1-.e16.
27. Shu J, Xie W, Mei C, Ren A, Ke S, Ma M, et al. Safety and clinical efficacy of Relmacabtagene autoleucel (relma-cel) for systemic lupus erythematosus: a phase 1 open-label clinical trial. EClinicalMedicine. 2025;83:103229.
28. UPDATED: Novartis halts autoimmune CAR-T trials after 3 deaths, as BMS also pauses studies [updated August 31, 2026. Available from: https://www.fiercebiotech.com/biotech/novartis-bristol-myers-squibb-halt-car-t-cell-trials-due-immune-events.
29. Novartis, Bristol Myers pause autoimmune CAR-T trials due to safety concerns [updated Sept. 1, 2026. Available from: https://www.biopharmadive.com/news/novartis-bristol-myers-autoimmune-cell-therapy-trial-halt/829218/.
30. Ellebrecht CT, Bhoj VG, Nace A, Choi EJ, Mao X, Cho MJ, et al. Reengineering chimeric antigen receptor T cells for targeted therapy of autoimmune disease. Science. 2016;353(6295):179–84.
31. Lee J, Lundgren DK, Mao X, Manfredo-Vieira S, Nunez-Cruz S, Williams EF, et al. Antigen-specific B cell depletion for precision therapy of mucosal pemphigus vulgaris. J Clin Invest. 2020;130(12):6317–24.
32. Oh S, Mao X, Manfredo-Vieira S, Lee J, Patel D, Choi EJ, et al. Precision targeting of autoantigen-specific B cells in muscle-specific tyrosine kinase myasthenia gravis with chimeric autoantibody receptor T cells. Nat Biotechnol. 2023;41(9):1229–38.
33. Reincke SM, von Wardenburg N, Homeyer MA, Kornau HC, Spagni G, Li LY, et al. Chimeric autoantibody receptor T cells deplete NMDA receptor-specific B cells. Cell. 2023;186(23):5084-97.e18.
34. Nicchia GP, Mastrototaro M, Rossi A, Pisani F, Tortorella C, Ruggieri M, et al. Aquaporin-4 orthogonal arrays of particles are the target for neuromyelitis optica autoantibodies. Glia. 2009;57(13):1363–73.
35. Crane JM, Lam C, Rossi A, Gupta T, Bennett JL, Verkman AS. Binding affinity and specificity of neuromyelitis optica autoantibodies to aquaporin-4 M1/M23 isoforms and orthogonal arrays. J Biol Chem. 2011;286(18):16516–24.

36. Iorio R, Fryer JP, Hinson SR, Fallier-Becker P, Wolburg H, Pittock SJ, et al. Astrocytic autoantibody of neuromyelitis optica (NMO-IgG) binds to aquaporin-4 extracellular loops, monomers, tetramers and high order arrays. J Autoimmun. 2013;40:21–7.
37. Pisani F, Mastrototaro M, Rossi A, Nicchia GP, Tortorella C, Ruggieri M, et al. Identification of two major conformational aquaporin-4 epitopes for neuromyelitis optica autoantibody binding. J Biol Chem. 2011;286(11):9216–24.
38. Owens GP, Ritchie A, Rossi A, Schaller K, Wemlinger S, Schumann H, et al. Mutagenesis of the aquaporin 4 extracellular domains defines restricted binding patterns of pathogenic neuromyelitis optica IgG. J Biol Chem. 2015;290(19):12123–34.
39. Soltys J, Liu Y, Ritchie A, Wemlinger S, Schaller K, Schumann H, et al. Membrane assembly of aquaporin-4 autoantibodies regulates classical complement activation in neuromyelitis optica. J Clin Invest. 2019;129(5):2000–13.
40. Gupta M, Khandelwal NK, Nelson A, Hwang P, Pourmal S, Bennett JL, et al. Structural basis of aquaporin-4 autoantibody binding in neuromyelitis optica. Sci Adv. 2025;11(8):eadq7560.
41. Rosenbaum M, Andreani V, Kapoor T, Herp S, Flach H, Duchniewicz M, et al. MZB1 is a GRP94 cochaperone that enables proper immunoglobulin heavy chain biosynthesis upon ER stress. Genes Dev. 2014;28(11):1165–78.
42. O'Connor BP, Raman VS, Erickson LD, Cook WJ, Weaver LK, Ahonen C, et al. BCMA is essential for the survival of long-lived bone marrow plasma cells. J Exp Med. 2004;199(1):91–8.
43. Kumar M, Keller B, Makalou N, Sutton RE. Systematic determination of the packaging limit of lentiviral vectors. Hum Gene Ther. 2001;12(15):1893–905.
44. Slabik C, Kalbarczyk M, Danisch S, Zeidler R, Klawonn F, Volk V, et al. CAR-T Cells Targeting Epstein-Barr Virus gp350 Validated in a Humanized Mouse Model of EBV Infection and Lymphoproliferative Disease. Mol Ther Oncolytics. 2020;18:504–24.
45. Workman P, Aboagye EO, Balkwill F, Balmain A, Bruder G, Chaplin DJ, et al. Guidelines for the welfare and use of animals in cancer research. Br J Cancer. 2010;102(11):1555–77.

Figures

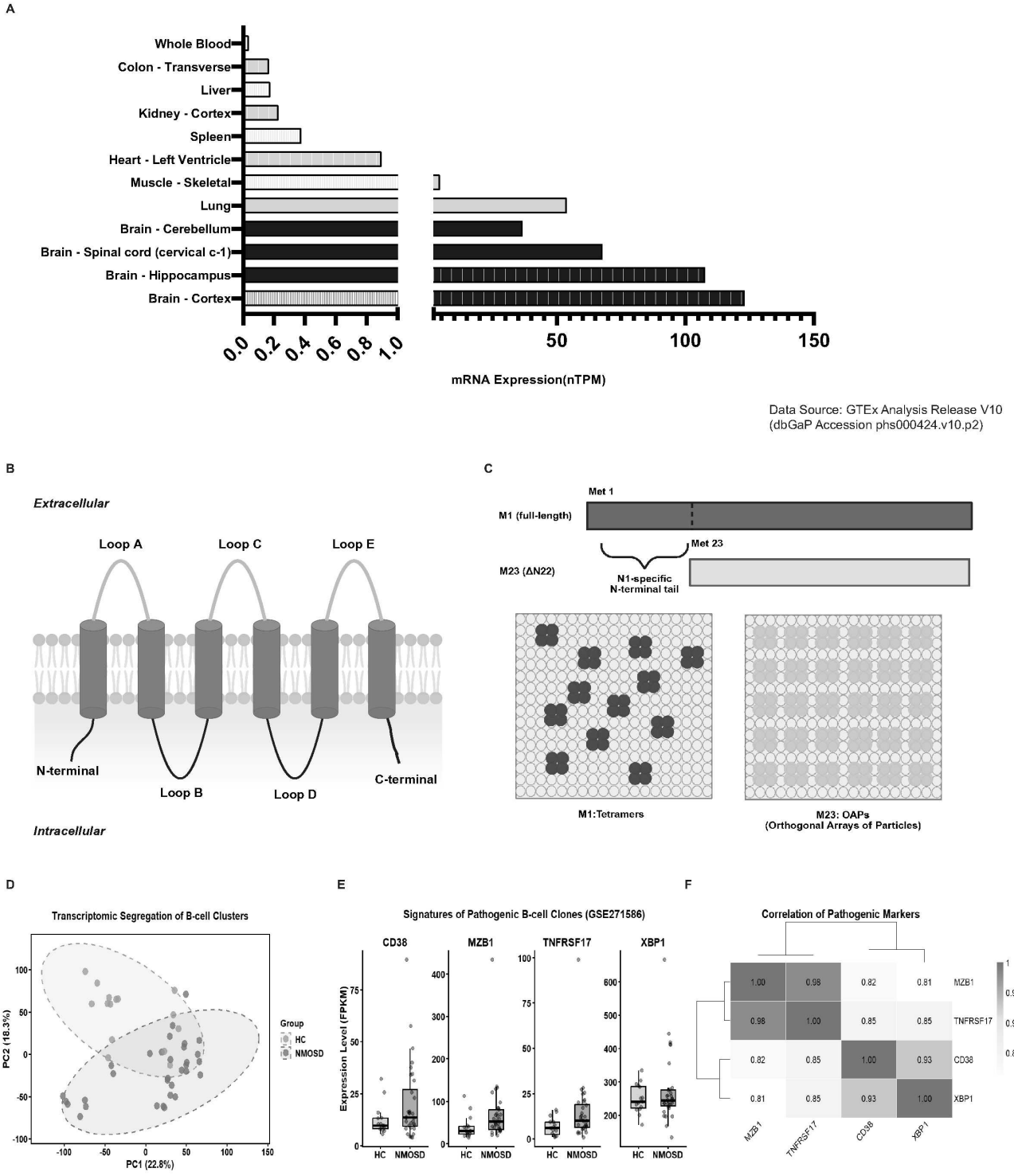


Figure 1

AQP4 exhibited CNS-specific expression and defined a coordinated pathogenic B-cell program in NMOSD

(A) Tissue-specific expression profiling of AQP4.

Gene expression of AQP4 reported by Genotype Tissue Expression(GTEx) database.

Expression values are shown in Transcripts Per Kilobase Million mapped reads (TPM).

(B) Structure of the AQP4 monomer.

A two-dimensional schematic illustrating the six-transmembrane (6-TM) helices and the orientation of extracellular loops (A, C, and E) relative to the plasma membrane. Created in BioRender.

(C) Molecular characterization and supramolecular membrane organization of AQP4 isoforms.

Schematic illustrating the N-terminal differences between M1 and M23 isoforms and their distribution patterns as individual tetramers or orthogonal arrays of particles (OAPs) on the cell membrane. Created in BioRender.

(D) Principal Component Analysis (PCA) of B-cell transcriptomes.

Spatial segregation of B-cell clusters between healthy controls (HC) and NMOSD patients based on the GSE271586 dataset. Variance explained by PC1 and PC2 is indicated on the axes.

(E) Expression profiling of pathogenic B-cell signatures.

Normalized FPKM values of *CD38*, *MZB1*, *TNFRSF17* (BCMA), and *XBP1* in purified B cells from NMOSD patients compared to healthy controls. Data were presented as mean ± SEM.

(F) Correlation matrix of B-cell pathogenic markers.

Pearson correlation coefficients () calculated for the expression levels of *CD38*, *MZB1*, *TNFRSF17*, and *XBP1* within the NMOSD patient cohort.

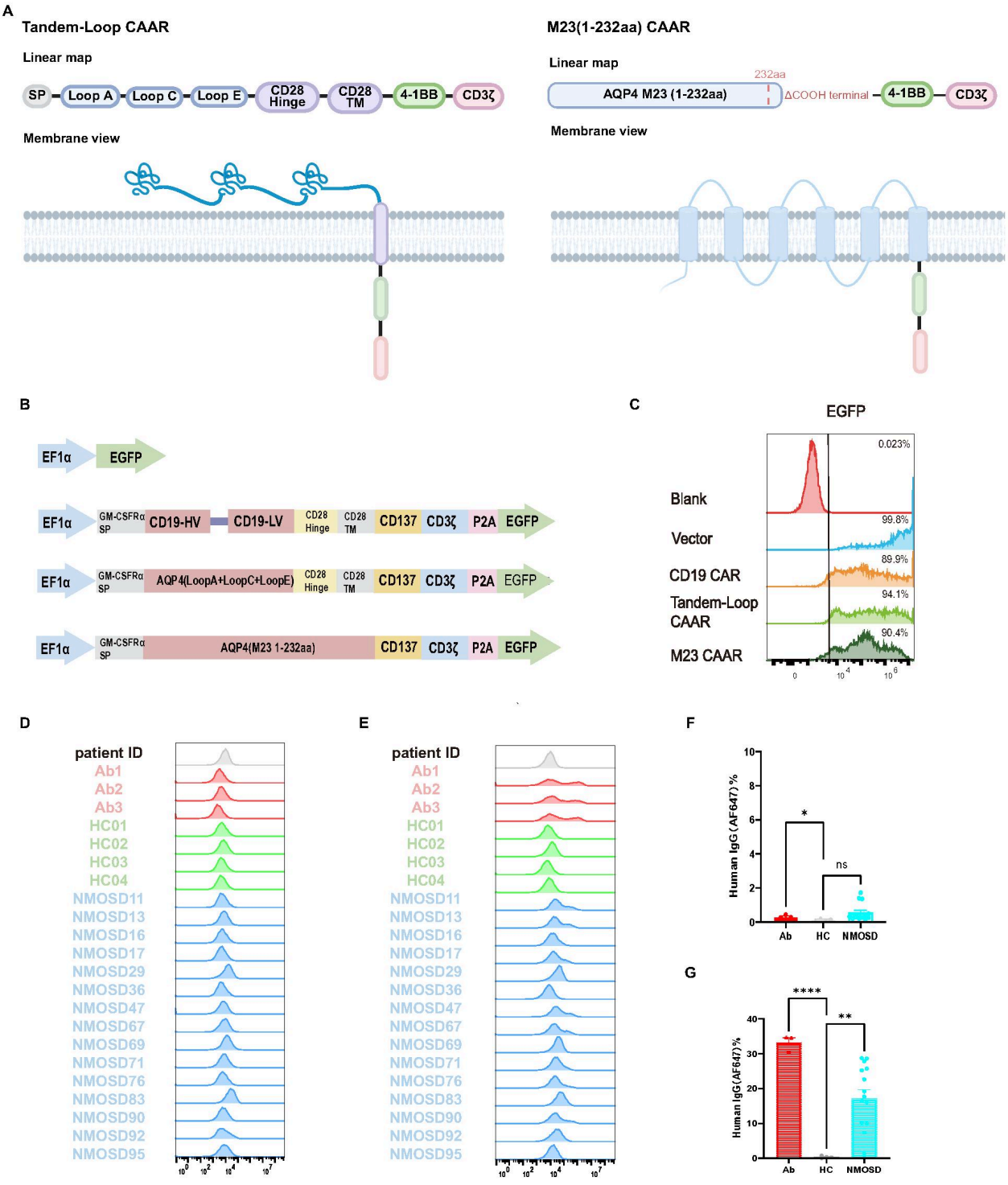


Figure 2

M23-CAAR construct specifically captured clinical autoantibodies

(A) Schematic of AQP4-CAAR constructs.

Schematic representation of the two receptor designs: the “Tandem-Loop CAAR,” featuring AQP4 extracellular loops A, C, and E linked in series; and the “M23 CAAR,” utilizing the native-conformation M23 isoform (residues 1-232). Both constructs were fused to CD137(4-1BB)-CD3 signaling chains. Created in BioRender.

(B) Schematic of lentiviral transfer plasmids.

Linear maps of the four expression vectors used in this study: Vector control (EGFP only), CD19-targeted CAR, Tandem-Loop CAAR, and M23 CAAR. All constructs are driven by the EF1 promoter and include a P2A-EGFP reporter for tracking expression. SP, signal peptide. TM, transmembrane domain.

(C) Expression efficiency in HEK293T cells.

The transfection efficiency of HEK293T cells was measured 36h after transfection by C-flow cytometry, as monitored by EGFP fluorescence.

(D-E) Specific binding to NMOSD patient autoantibodies.

Histograms show IgG binding of human serum to 293T cells expressing Tandem-Loop CAAR(D) or M23 CAAR(E) as determined by flow cytometry. Ab1-3 refers to three autontibodies derived from NMOSD patients. Serum of NMOSD patients were shown in blue and sera of healthy controls were shown in green, Autoantibodies were shown in ren, respectively.

(F–G) Statistical quantification of clinical recognition.

Summary statistics of binding efficiencies across multiple clinical serum samples for (F) Tandem-Loop CAAR (quantifying data from 2D) and (G) M23-CAAR (quantifying data from 2E). The data were presented as mean $\pm$ SEMs. ns, no significant difference, *$p < 0.05$, **$p < 0.01$, ****$p< 0.0001$, unpaired t test.

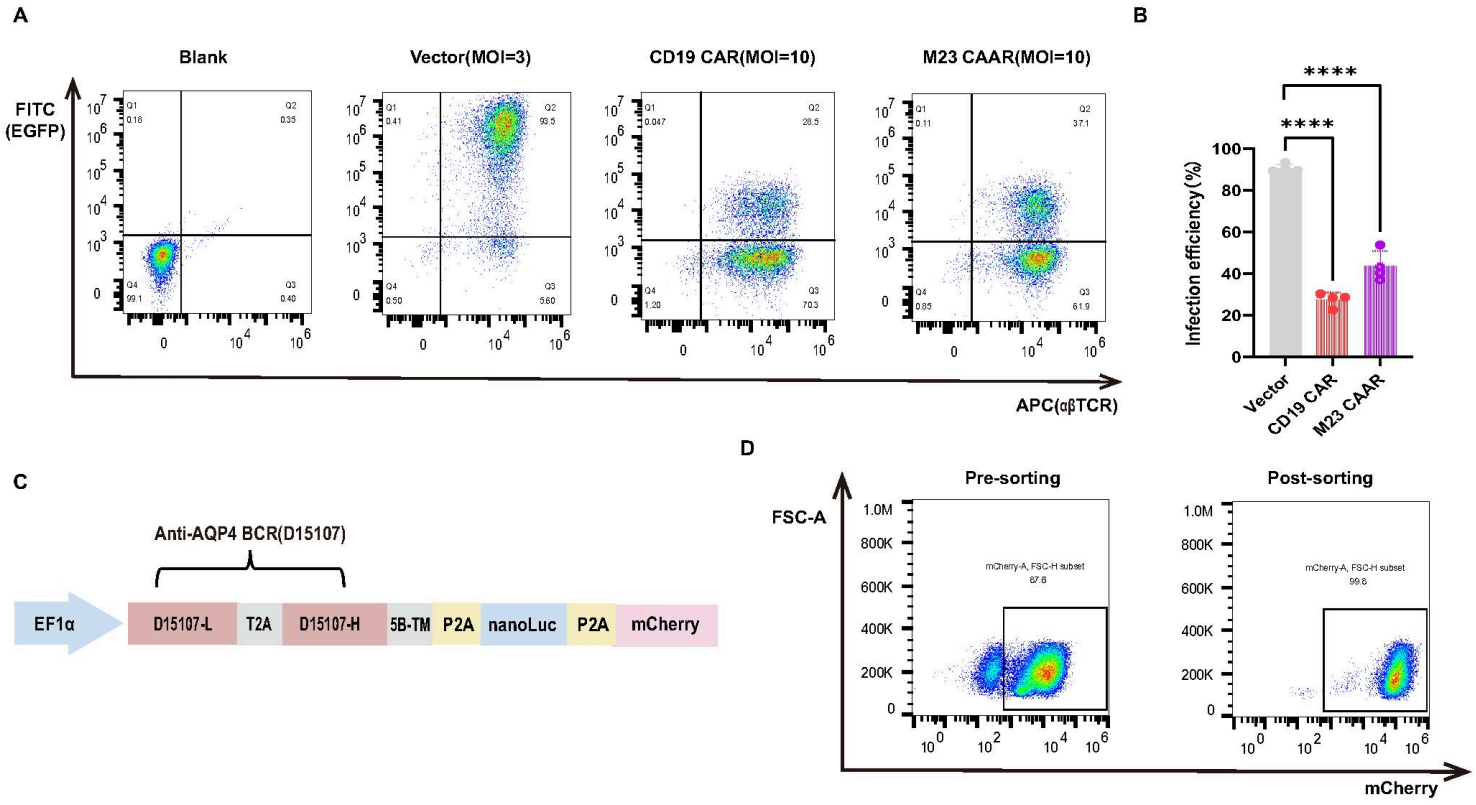


Figure 3

Successful establishment of the CAAR-T effector and pathogenic B-cell target system

(A–B) Engineering of primary human CAAR-T cells.

(A) Representative flow cytometry plots of lentivirus infection efficiency on day 8.

(B) Statistical quantification of transduction efficiency of lentivirus infection of human primary T cells on day 8 across four independent donors (=4). The data were presented as the means ± SEMs. ****p< 0.0001, unpaired t test.

(C) Schematic design of the pathogenic B-cell model.

Map of the transfer plasmid encoding a membrane-anchored, full-length human IgG-BCR (D15107 sequence). The construct included a CD5b-transmembrane domain for surface anchoring and co-expresses nano-Luciferase and mCherry for downstream cytotoxicity assays.

(D) Purity validation of target Nalm6 cells.

Flow cytometric analysis of mCherry expression in D15107-Nalm6 target cells before and after FACS-mediated enrichment.

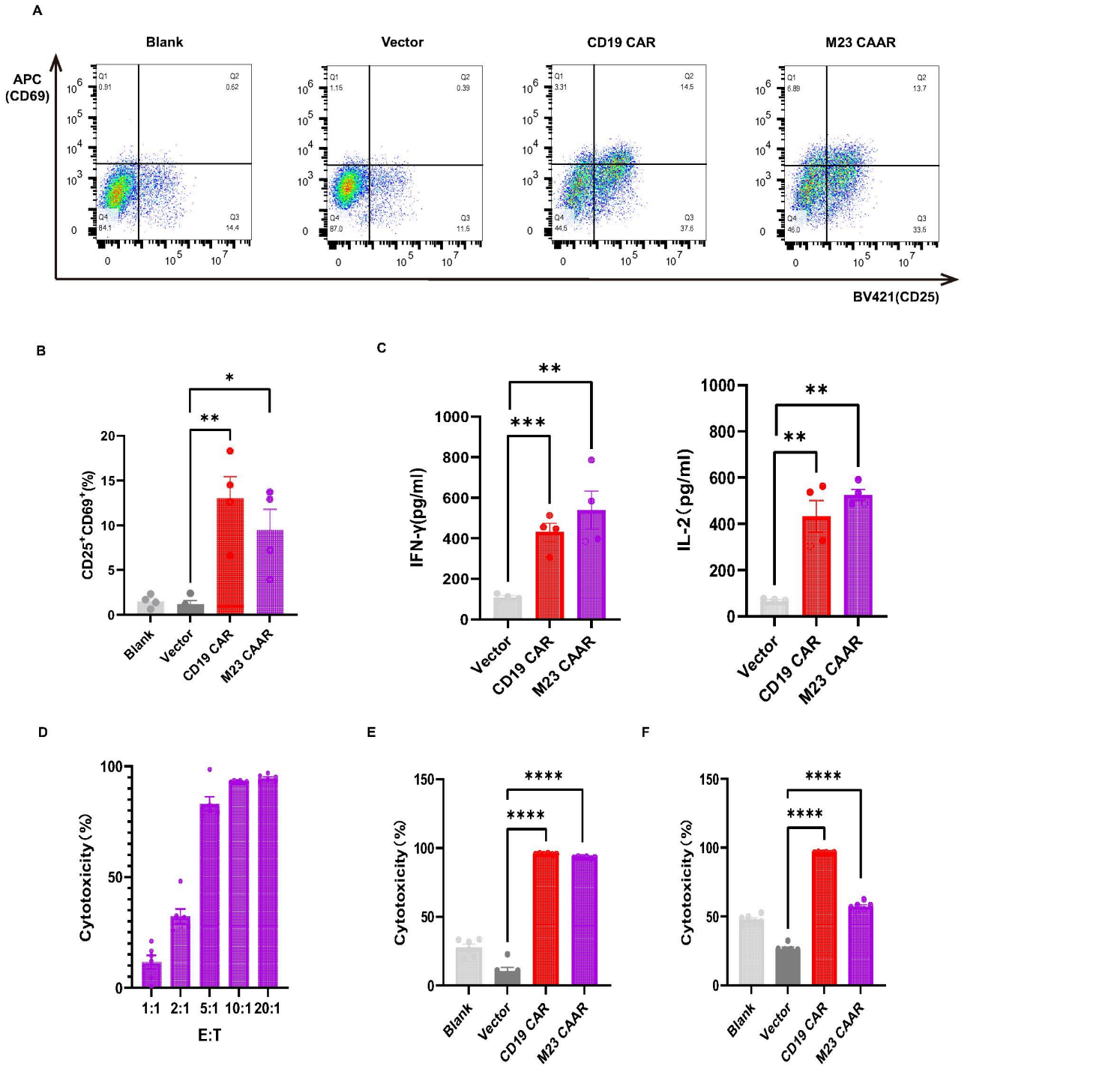


Figure 4

M23 CAAR-T cells undergo potent antigen-driven activation and exhibited highly selective cytotoxicity against pathogenic B-cell models

(A–B) Antigen-specific T-cell activation.

(A) Representative flow cytometry plots of activation markers CD25 and CD69 on M23 CAAR T cells following 16-hour co-culture with D15107-Nalm6 target cells. The ratio of effector cells to target cells was 5:1.

(B) Statistical quantification of activation marker expression across four independent experiments (=4). The data are presented as the means ± SEMs. *p < 0.05, **p < 0.01, by a two-tailed unpaired t-test.

(C) Secretory profile of effector cytokines.

ELISA quantification of Interferon-gamma (IFN-) and Interleukin-2 (IL-2) levels in the supernatants of CAAR-T cells co-cultured with target cells for 16 h. The ratio of effector cells to target cells was 5:1 (n=4). The data was presented as the means ± SEMs. ** p < 0.01, *** p < 0.001, by a two-tailed unpaired t-test.

(D)In vitro cytolytic potency across varying E:T ratios. Potent cytotoxicity of M23 CAAR-T cells against D15107-Nalm6 target cells was measured using a luciferase-based killing assay at multiple effector-to-target (E:T) ratios. The coincubation time of the effector cells and target cells was 16 h. The data are presented as the means ± SEMs.

(E)The cytotoxic activity of different effector cells against D15107-Nalm6 target cells was evaluated by luciferase-based killing assay at the effector-to-target (E:T) ratio of 10:1. The coincubation time was 16 h. The data are presented as the means ± SEMs. ****p< 0.0001, by a two-tailed unpaired t-test.

(F) Evaluation of antigen-dependent selectivity. Potent cytotoxicity of M23 CAAR-T cells against Nalm6 cells was measured using a luciferase-based killing assay at the effector-to-target (E:T) ratio of 10:1. The coincubation time of the effector cells and target cells was 16 h. The data was presented as the means ± SEMs. ****p< 0.0001, by a two-tailed unpaired t-test.

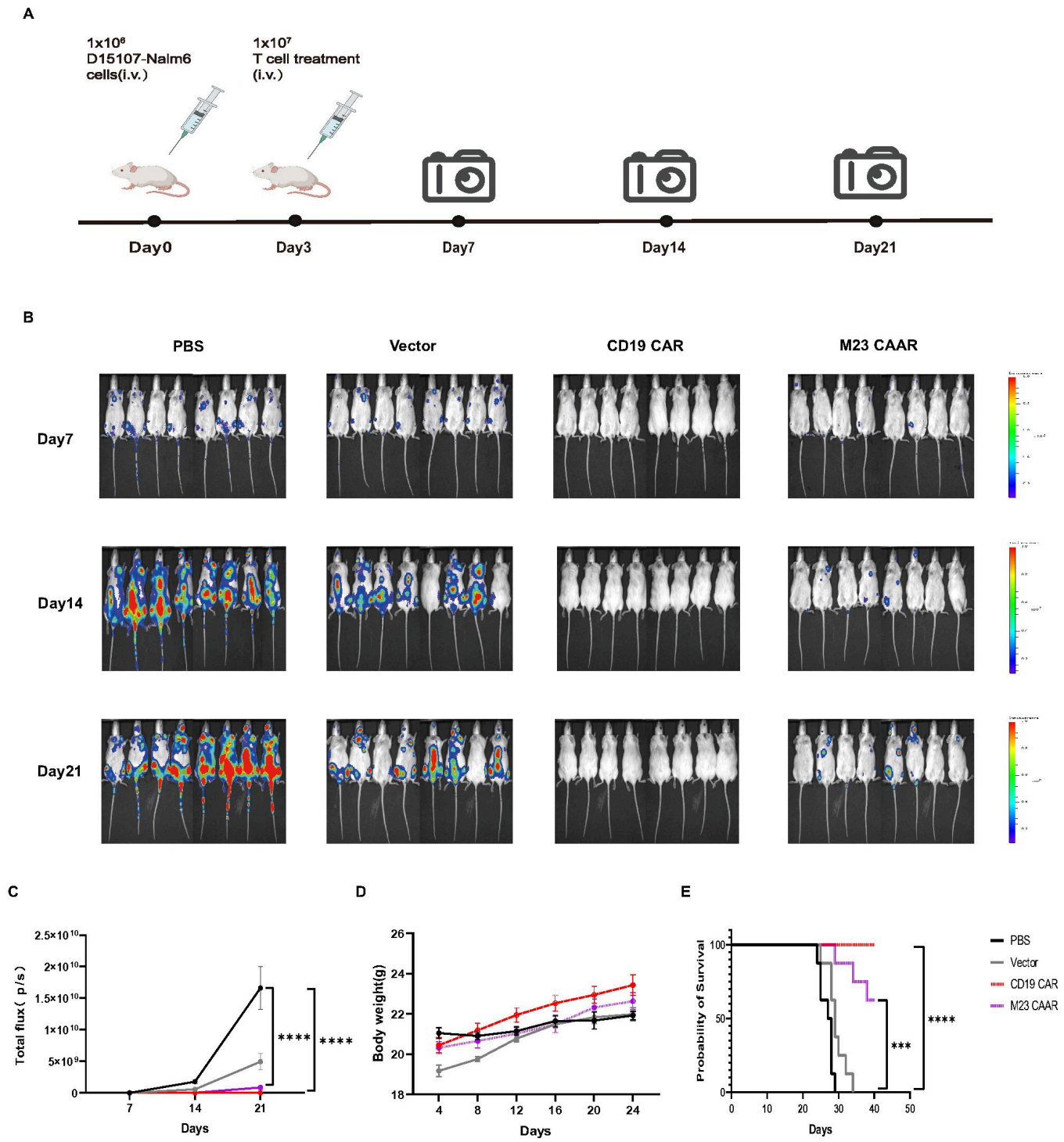


Figure 5

Systemic infusion of M23 CAAR-T cells induced durable clearance of pathogenic B cells and provided robust survival rescue in vivo

(A) Schematic of the animal experiment protocol. Timeline of the NMOSD xenograft model established in NSG mice. A total of 1x10^6 D15107-Nalm6 target cells were inoculated intravenously on Day 0,

followed by a single infusion of PBS, Vector-T cells, CD19 CAR-T cells or M23 CAAR-T cells on Day 3. Each mouse was inoculated with 1×10^7 cells intravenously. Monitor the luminescence of animals on day7, day 14 and day 21.

(B) Representative bioluminescence imaging (BLI). Bioluminescence imaging with an IVIS Spectrum system.

(C) Quantification of tumor burden. Statistical analysis of total bioluminescent flux (photons/second) over time via in vivo imaging after treatment. The data are presented as the means ± SEMs. *** $p < 0.001$, ****$p < 0.0001$, as determined by a two-tailed unpaired t-test.

(D) Body weight changes in the mice during treatment. The data are presented as the means ± SEMs.

(E) Survival curves. Kaplan-Meier survival curves comparing mice treated with CD19 CAR-T cells or M23 CAAR-T cells versus PBS group. *** $p < 0.001$, ****$p < 0.0001$, Log-rank test.

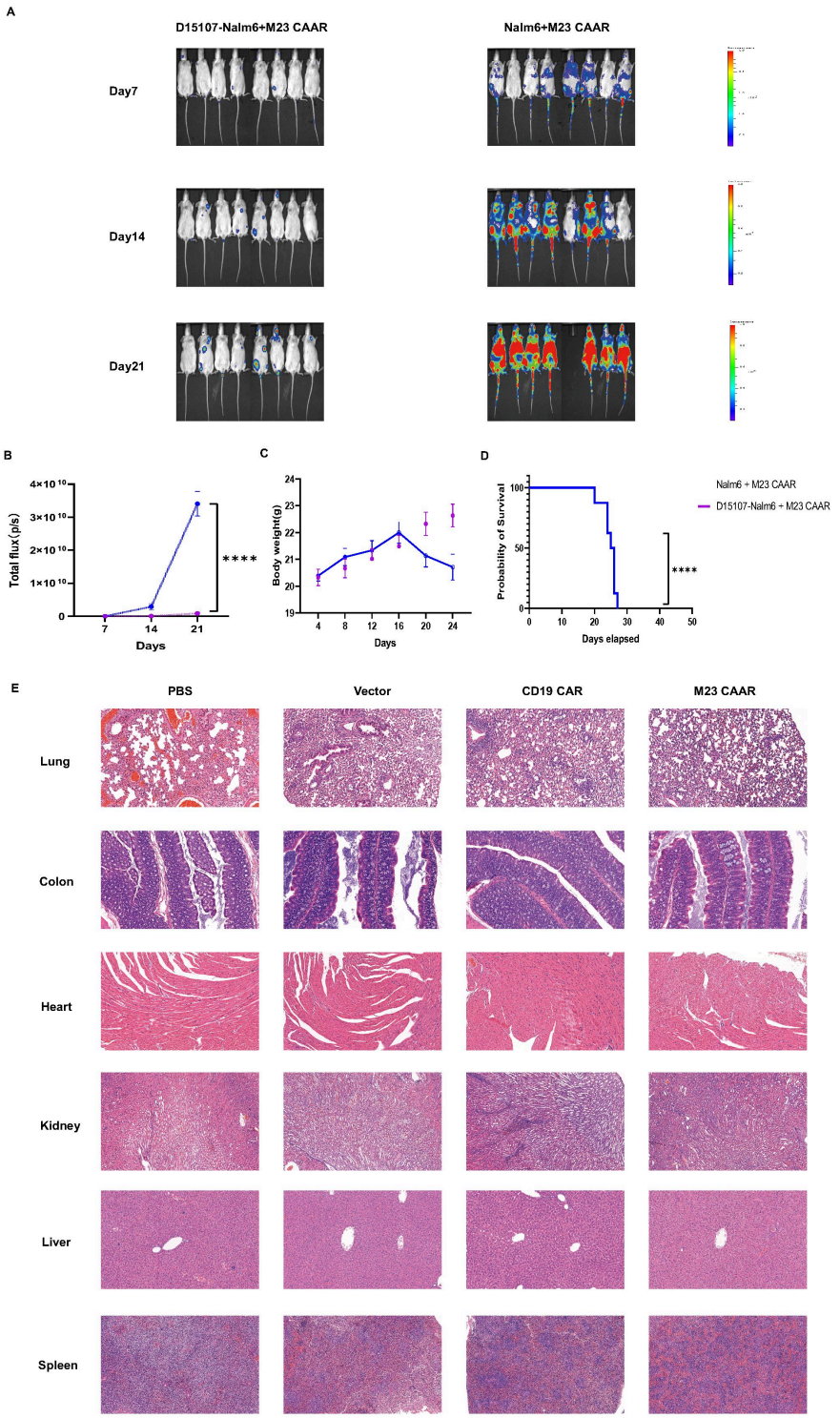


Figure 6

M23 CAAR-T cells maintained a favorable systemic safety profile

(A–B) Evaluation of in vivo specificity in an antigen-negative model.

(A) Longitudinal monitoring of systemic B-cell burden via bioluminescence imaging (BLI).

(B) Statistical analysis of total bioluminescent flux (photons/second) over time via in vivo imaging after treatment. The data are presented as the means ± SEMs. ****p < 0.0001, as determined by a two-tailed unpaired t-test.

(C) Body weight changes in the mice during treatment. The data are presented as the means ± SEMs.

(D) Survival curves of the mice. ****p < 0.0001, Log-rank test.

(E) Systematic histopathological evaluation. Representative Hematoxylin and Eosin (H&E) staining of major organs—including the heart, liver, spleen, lung, and kidney—harvested at the study endpoint.

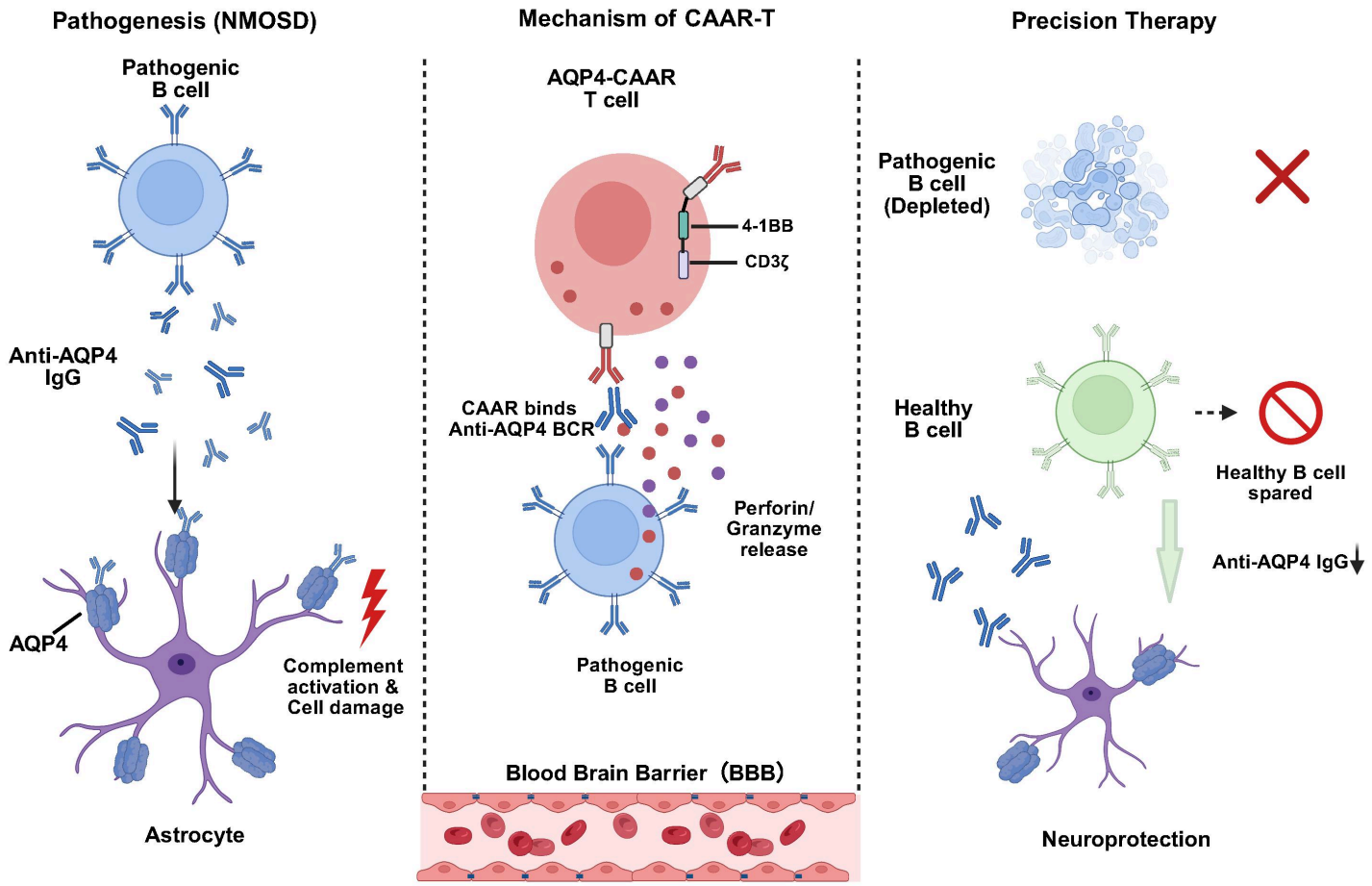


Figure 7

AQP4-CAAR T cells function as a precision "molecular decoy" to reset immunological tolerance in NMOSD

Schematic summary of NMOSD pathogenesis and the selective depletion of pathogenic B cells by AQP4-CAAR T cells. Left, AQP4-reactive B cells generate pathogenic AQP4-IgG, which binds AQP4 on astrocytes and promotes complement-mediated cellular injury. Middle, M23 AQP4 displayed on CAAR-T

cells acts as a molecular decoy that engages anti-AQP4 B-cell receptors and triggers selective cytotoxicity against autoreactive B cells. Right, depletion of AQP4-reactive B-cell clones, with relative sparing of antigen-negative B cells, is proposed to reduce pathogenic autoantibody production and limit further astrocyte injury while preserving broader humoral immunity.Created in BioRender.

Supplementary Files

This is a list of supplementary files associated with this preprint. Click to download.

- SupplementaryInformation.docx
- Unprocessedoriginalimages.docx
- FigureS1.pdf
- FigureS2.pdf